Nanoscale Advances

ROYAL SOCIETY OF CHEMISTRY

PAPER

View Article Online
View Journal | View Issue

Cite this: *Nanoscale Adv.*, 2025, **7**, 2351

Novel synthesis approach for highly crystalline $CrCl_3/MoS_2$ van der Waals heterostructures unaffected by strain†

Mahmoud M. Hammo, *[ab] Samuel Froeschke, [a] Golam Haider, [a] Daniel Wolf, [a] Alexey Popov, [a] Bernd Büchner, [ac] Michael Mertig [bd] and Silke Hampel [a]

Received 13th November 2024
Accepted 21st February 2025

DOI: 10.1039/d4na00935e

rsc.li/nanoscale-advances

Controlling the layer-by-layer chemistry and structure of nanomaterials remains a crucial focus in nanoscience and nanoengineering. Specifically, the integration of atomically thin semiconductors with antiferromagnetic two-dimensional materials holds great promise for advancing research. In this work, we successfully demonstrate a new synthesis approach for high-crystallinity $CrCl_3/MoS_2$ van der Waals heterostructures *via* a thermodynamically optimized chemical vapor transport (CVT) process on *c*-sapphire (0001) substrates. The 2H-MoS_2 layers can be grown as monolayers or with varying twist angles whereas the deposition of $CrCl_3$ layers in a second step forms the well-defined heterostructure. Of particular significance are the sharp and clean edges and faces of the crystals, indicating high-quality interfaces in the heterostructures. Raman spectroscopy, AFM and HRTEM confirm the monocrystalline character and precise structure of these layered nanomaterials, in which their intrinsic properties are preserved and unaffected by strain. This can pave the way for next-generation applications, particularly in valleytronics, opto-spintronics, and quantum information processing.

Introduction

The exceptional properties of van der Waals (vdW) heterostructures, which comprise atomically thin layered materials such as graphene, transition metal trihalides (TMTHs), transition metal dichalcogenides (TMDCs) and various topologically layered materials, have paved the way for a wide range of innovative research opportunities, encompassing both fundamental and applied research.[1–6] These heterostructures are predominantly created by stacking two-dimensional (2D) materials layer-by-layer. The weak vdW forces enable the assembly of dissimilar materials without the constraints of lattice matching.[7] A number of studies have demonstrated that the incorporation of a monolayer (ML) of TMDCs into 2D materials, including $WSe_2/CrBr_3$, can lead to a notable alteration in their optoelectronic properties.[8–12] However, the synthesis of strain-free heterostructures remains an intriguing area of study. By employing a synthesis method that mitigates strain, we ensure that the intrinsic properties of layers are preserved, resulting in high-quality interfaces with minimal defects. The strain-free synthesis method is driven by its significance for practical applications, particularly in valleytronics, opto-spintronics, and quantum information processing. In valleytronic devices, the ability to manipulate electron populations in distinct energy valleys of 2D semiconductors such as MoS_2 is crucial. Strain-induced distortions can shift these valleys, reducing device efficiency and stability.[13] The strain-free growth ensures that the valleys remain well-defined, enabling robust valley-dependent charge transport and optical transitions. In addition to the well-studied heterostructure $WSe_2/CrBr_3$, the construction and investigation of the similar heterostructure $CrCl_3/MoS_2$ is also very promising, for example, to explore phenomena such as the spin proximity effect. The combination of a 2D semiconductor (MoS_2) and a layered A-type antiferromagnetic insulator ($CrCl_3$)[14–16] forms a promising heterostructure for opto-spintronics. The direct bandgap of MoS_2 supports efficient light emission and absorption, while $CrCl_3$ provides magnetic ordering. This enables optical control of spin and valley degrees of freedom, paving the way for spin-based photonic devices and memory elements.[17] Therefore, the

[a]*Leibniz Institute for Solid State and Materials Research Dresden, Helmholtzstraße 20, 01069 Dresden, Germany. E-mail: m.hammo@ifw-dresden.de; Tel: +49 17687315637*
[b]*Institute of Physical Chemistry, Technische Universität Dresden, 01062 Dresden, Germany*
[c]*Institute of Solid State and Materials Physics, Technische Universität Dresden, Dresden, Germany*
[d]*Kurt-Schwabe-Institut für Mess- und Sensortechnik Meinsberg e.V., Kurt-Schwabe-Straße 4, Waldheim 04736, Germany*

† Electronic supplementary information (ESI) available: Further details on the CVT synthesis process and workflow are provided, encompassing stepwise procedures, reaction conditions, and optimizations made. Additionally, the purification method for commercial $CrCl_3$ is outlined. Substrate pretreatment techniques, such as cleaning procedures and surface modifications, are also described. See DOI: https://doi.org/10.1039/d4na00935e

combination of these types of materials continues to generate significant interest among physicists, chemists and material scientists,[18–21] and represents an effective approach to developing highly functional materials for spintronic and opto-spintronic applications.[19,22] High-quality, strain-free interfaces are essential for fabricating devices that leverage quantum coherence. In heterostructures where spin–orbit coupling or exciton recombination is involved, strain can introduce unwanted decoherence or scatter carriers.[23]

Two principal approaches are typically applied for the fabrication of vdW heterostructures. The first one is a top-down approach, which encompasses techniques such as exfoliation from the bulk/single crystal and subsequent assembly through the utilization of standard dry transfer techniques.[18–20,24–27] This approach does not allow for precise control over the number of layers, which limits its overall significance. In addition to being time-consuming, this approach presents other disadvantages, including damage to the edge structure and contamination of the cleaved interfaces. Furthermore, the presence of process-related impurities at the interface, including polymer residues,[28] water and air bubbles,[29] impedes the efficient formation of heterostructures. This significantly affects the overall quality of the heterostructure.[30]

The second approach is a bottom-up method, in which such heterostructures are commonly grown using techniques such as chemical vapor deposition (CVD),[31,32] physical vapor deposition (PVD),[33] or various epitaxial processes. These methods are particularly well-suited for the production of heterostructures with high-quality, clean, and atomically sharp interfaces. While the synthesis *via* CVD or PVD requires rather complex equipment, the synthesis *via* CVD is a highly cost-effective and straightforward process. Instead of these methods, and for the first time, sequential chemical vapor transport (CVT) was employed to prepare 2D vdW heterostructures. Sequential CVT comprises two consecutive steps. Each step is designed to achieve a specific part of the total vdW heterostructure growth. The optimal parameters (*e.g.* precursor deposition, temperature gradient ΔT, residence time and transport time) have to be identified for each individual step.

This study describes a scalable two-step vapor phase growth process for the fabrication of highly crystalline, vertically stacked $CrCl_3/MoS_2$ heterostructures on *c*-sapphire (Al_2O_3) substrates oriented along the (0001) direction. Different growth temperatures and times have been evaluated, and the best conditions have been identified. Theoretical studies of gas phase composition and equilibria support the experimental performance. The resulting heterostructures were analyzed by optical microscopy, atomic force microscopy (AFM), Raman spectroscopy and high-resolution transmission electron microscopy (HRTEM). Of particular significance are the sharp and clean edges and faces of the crystals, indicating high-quality interfaces of the heterostructures.

Experimental section

Materials

$CrCl_3$ (Alfa Aesar, anhydrous 99.9%), MoO_3 (99.9995%, thermo scientific, melting point: 795 °C), S (metals basis 99.9995%, thermo scientific, boiling point: ~445 °C), and KCl (99.999%, Sigma Aldrich).

Thermodynamic simulations using TRAGMIN software

Thermodynamic simulations were performed with a modified version of the software "TRAGMIN 5.1". The used thermodynamic data of all species were taken from the FactPS database[34] and a list of the used species is given in the ESI.† A system volume of 9.4 mL was used, and 5×10^{-9} mmol H_2O and 1×10^{-9} mmol Ar traces were added for all simulations.

Preparation and pretreatment of substrates

The (0001) plane of *c*-sapphire wafers were cut into substrates with specific dimensions ($10.0 \times 5 \times 0.5$ mm^3). A photoresist was spun onto the wafers to protect the polished surface from damage during the cutting process. To remove the photoresist afterwards, the substrates were rinsed with acetone and cleaned by ultrasonic treatment in distilled water for 15 min. Afterwards, they were rinsed again with distilled water and excess liquid was removed with compressed nitrogen. Finally, the substrates were annealed in air as described in Fig. S1.†

Synthesis of $CrCl_3/MoS_2$ by sequential CVT

For the synthesis of MoS_2 nanolayers, the starting materials were mixed in a glovebox with the ratio $MoO_3 : S = 1 : 2$. One milligram of this mixture was placed on the source side of the ampoule, with approximately 1 milligram of KCl utilized as the transport agent. A *c*-sapphire (0001) substrate was positioned on the sink side of the ampoule and sealed using a vacuum sealing line (oxyhydrogen flame) at a pressure of $\sim 2 \times 10^{-3}$ mbar. For the growth process, a two-zone LOBA furnace (HTM Reetz, GmbH) was set to the following temperatures $T_1 = 1000$ °C; $T_2 = 800$ °C for 30 min, followed by natural cooling. The ampoules were opened in the glovebox, and the substrate was transferred to a new ampoule. In the second ampoule, approximately 5 milligrams of $CrCl_3$ were placed on the source side and the substrate was transferred to the sink side. The growth conditions for the second step were 600 °C at the source side and 500 °C at the sink side as shown in Fig. S2.† The ampoule was quenched in water after 15 min.

Preparation of the TEM lamella

To analyze the cross-section of the $CrCl_3/MoS_2$ heterostructure using TEM, a lamella in the overlapped region of the $CrCl_3/MoS_2$ heterostructure was prepared by focused ion beam (FIB) cutting. The preparation was carried out using a Helios 5 CX (Thermo Scientific). Initially, the sample was coated with a 20 nm carbon layer using a sputter coater, followed by electron beam-induced deposition (EBID) and ion beam-induced deposition (IBID) for additional protection and stability. The FIB cutting was performed at an acceleration voltage of 30 kV and a current of 2.5 nA to create the initial trenches, followed by a lower current for the final polishing to ensure minimal damage to the sample. This multi-step coating and cutting process ensured the sample's integrity during FIB milling and

subsequent TEM analysis. The precise FIB technique allowed for the accurate extraction of a thin lamella, which is crucial for detailed cross-sectional TEM studies.

Characterization

Optical microscopy. After breaking the ampoule, the first characterization of the crystal morphology was conducted using an optical microscope (Keyence VHX-7000) equipped with a VHX-7020 CMOS image sensor.

Scanning electron microscopy (SEM) and energy dispersive X-ray spectroscopy (EDX). Morphological and compositional analyses were performed using scanning electron microscopy (SEM) at various magnifications, coupled with energy dispersive X-ray spectroscopy (EDX) using an FEI Nova-NanoSEM 200. The EDAX Genesis Spectrum software was used to measure the composition of the crystals. 5 measurements at different spots/crystals were averaged to calculate the composition of each crystal or experiment.

Raman spectroscopic investigations. These measurements were performed using a T64000 Raman Spectrometer (Horiba Jobin Yvon) under 532 nm laser excitation. The spectra were recorded at room temperature utilizing an 1800 g mm^{-1} grating.

Transmission electron microscopy (TEM). As-grown MoS_2 layers were transferred onto TEM grids (Lacey-carbon 200 mesh Cu, Plano GmbH). Briefly, MoS_2 on the *c*-sapphire (0001) substrate was immersed in 500 μL of pure ethanol and subjected to ultrasonic treatment for 10 min. Subsequently, several drops of the resulting solution were pipetted onto the TEM grid and allowed to air dry. Then the transferred crystals were examined under an optical microscope before TEM investigation. For the $CrCl_3/MoS_2$ heterostructure, the lamella was prepared by FIB cutting and then measured by TEM. The measurements were performed with a HRTEM "FEI Titan^3 80-300" (ThermoFisher Scientific Company), operated at an acceleration voltage of 300 kV, with selected area electron diffraction (SAED) conducted over an area of a few nm.

Atomic force microscopy (AFM). Atomic force microscopy analysis was conducted in tapping mode under ambient conditions using TESPA-V2 tips on a "Dimension ICON" with ScanAsyst (Bruker, USA). Data analysis was conducted using the "Nanoscope Analysis" software, version 1.8.

Theoretical basis

To investigate the thermodynamic stability of two potential compounds in one system that are so different in their chemistry such as MoS_2 and $CrCl_3$, thermodynamic equilibrium calculations of the complex chemical systems with inclusion of the vapor phase have been performed. The initial results for the temperature-dependent vapor pressures and condensed phase stabilities of an equimolar $CrCl_3/MoS_2$ system are displayed in Fig. 1.

The calculation results demonstrate that, in principle, $CrCl_3$ and MoS_2 are stable next to each other over a wide temperature range suitable for the vapor phase growth of the desired

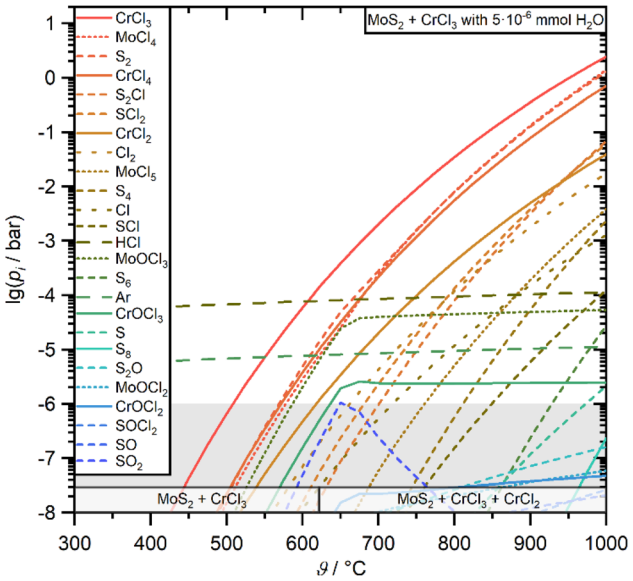

Fig. 1 Calculation results of the temperature-dependent vapor pressures of the dominant vapor species over an equimolar mixture of MoS_2 and $CrCl_3$ with traces of water. The predicted condensed phases at the bottom are displayed for amounts larger than 10^{-5} mmol. The grey area indicates vapor pressures that are too low to contribute to transport processes.

heterostructures. However above *ca.* 625 °C a significant decomposition of $CrCl_3$ to $CrCl_2$ sets in but has no major influence on the predicted vapor pressures.

Based on this initial assessment of the thermodynamic stability of the heterostructure, more detailed investigations of potential deposition strategies were performed. While studies on the individual deposition of ultrathin nanosheets of $CrCl_3$ by CVT have already been reported,[35–37] and can be adapted for the deposition of the first underlying layer of the heterostructure in a sequential deposition strategy, the optimization of the second deposition step on top of the first layer presents an even greater challenge due to the potentially much more complex chemical equilibria in the combined system. To understand this second potential deposition step and to estimate a suitable parameter window for following practical experiments, further calculations of thermodynamic equilibria were combined with CVT models to simulate the transport processes. The primary results for the investigated sequential deposition of $CrCl_3$ on MoS_2 are displayed in Fig. 2a. Despite the very small amount of MoS_2 used in this simulation to mimic a potentially thin layer of MoS_2 on the substrate, the simulations confirm that a regular deposition of $CrCl_3$ on MoS_2 should be possible at T_{source} above *ca.* 550 °C, similar to the individual deposition of $CrCl_3$ nanosheets.[35] The calculated transport efficiencies (Fig. 2b) further confirm that the transport process of $CrCl_3$ is dominated by sublimation and that, despite the relatively high partial pressures of Mo-containing vapor species (Fig. 2a), the transport process is not strongly interfered with.

The sequential transport in the opposite order (MoS_2 on $CrCl_3$) with the use of KCl as a transport agent could not be simulated properly because the use of KCl most likely generates

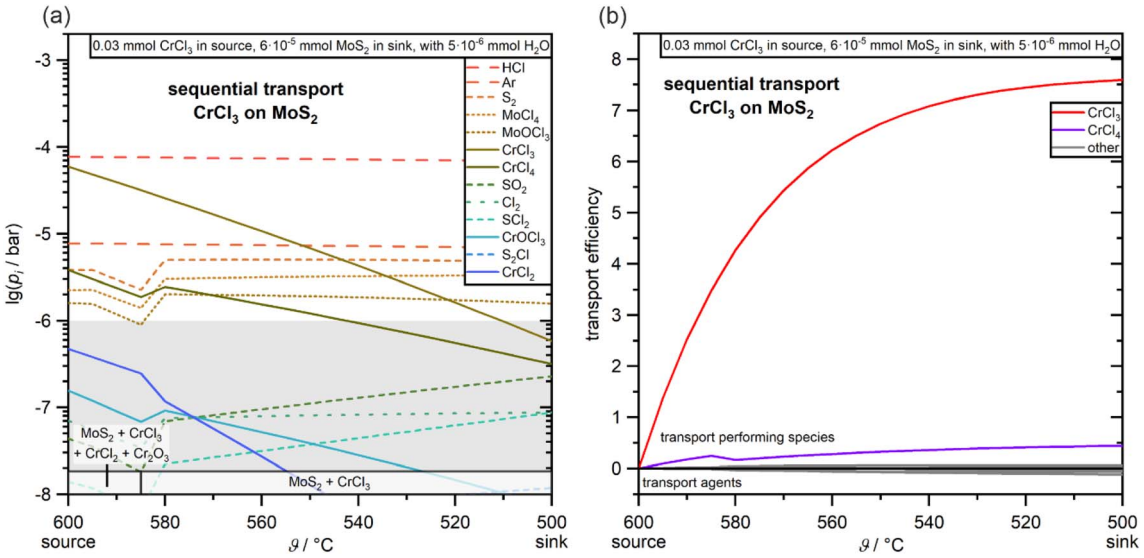

Fig. 2 (a) Temperature-dependent partial pressures and predicted deposited phases for the simulation of the sequential CVT heterostructure deposition of $CrCl_3$ (starting material in the source) on MoS_2 (starting material in the sink). For this simulation, the source temperature was fixed at 600 °C, while the temperature of the sink was varied between 595 and 500 °C. The grey area indicates vapor pressures that are too low to contribute to transport processes. (b) Calculated transport efficiencies for this simulated CVT.

vapor-phase complexes that are relevant for the transport process but are unknown with respect to both their exact structure and thermodynamic data.[38,39]

Results and discussion

Growth of MoS_2 as the bottom layer of the heterostructure

To optimize the growth of few-layer MoS_2 crystals as a bottom layer *via* CVT, the precursors molybdenum trioxide (MoO_3), sulfur (S) and potassium chloride (KCl) were used. We varied the synthesis temperatures (500 °C to 1000 °C), the temperature gradient (50–200 °C) and the transport time (5–60 min).

The optimal synthesis parameters include a heating rate of 10 K min^{-1}, with the temperature range maintained between 800 °C and 1000 °C for a duration of 30 min, followed by natural cooling (Fig. 3a). This specific heating rate ensures a controlled and uniform temperature increase, which is crucial for achieving the desired crystalline quality and thickness. Maintaining the synthesis temperature within this range for 30 min allows adequate material deposition and layer formation, promoting the growth of few-layer MoS_2 with minimal defects. The natural cooling process helps in stabilizing the crystal structure, thereby preserving the integrity and uniformity of the MoS_2 layers.

Characterization of MoS_2

The MoS_2 crystals are uniformly distributed across the substrate in various sizes and exhibit different shapes, including triangular, parallel (where triangular nanosheets stack at 0°), and anti-parallel (where triangular nanosheets stack at 60°). They are stable under ambient conditions. The lateral dimensions of the crystals vary from 10 to 60 μm. Optical images of selected crystals are shown in Fig. 3b and c. They exhibit sharp edges and show random twists at different angles: 0° (Fig. 3b) and 60° (Fig. 3c). The pale blue color resembles MoS_2 with few layers while the color gradually saturates with an increasing number of layers. Notably, under the same temperature gradient conditions, but using a longer transport time (more than one hour), the crystals will become thicker. Additionally, SEM images further support these observations, as shown in Fig. S3.†

TEM measurements were conducted to confirm the crystallinity and crystal structure. The bright-field TEM image in Fig. S5b† displays a MoS_2 flake, a few tens of nanometers thick, on the lacey carbon TEM grid. The mono-crystalline layer exhibits an almost hexagonal arrangement in this zone axis orientation (above the highlighted red line in Fig. 3d), whereas the superposition of two layers twisted by an in-plane rotation angle of 26° results in a prominent appearance of a so-called Moiré pattern (below the red line in Fig. 3d). In fact, the latter is confirmed by image simulations (see Fig. S6†) using the DrProbe software package,[40] incorporating the twist angle, which is determined from the Fourier transform (Fig. 3e) of the entire flake from which the HRTEM image in Fig. 3d is shown. The diffraction patterns (Fig. 3f,g) recorded at the 001 zone axis orientation exhibit individual reflections that confirm the high crystallinity of the samples. Specifically, the two lines in Fig. 3f cross two reflection pairs, indicating a twisted double layer of MoS_2 with a 13° twist angle. Similarly, three lines in Fig. 3g cross three reflection pairs, indicating a twisted multi-layer of MoS_2 with twist angles of 12° and 13°. HRTEM images of a similar flake, also taken at the 001 zone axis orientation (hexagonal space group 194) reveal a twisting between two MoS_2 layers, one extending until the upper edge and one ending 10 nanometers away from the edge. These observations, along with the measured *d*-spacing, confirm the high crystallinity and precise interlayer alignment of the MoS_2 flakes, validating the twisted bilayer and multilayer structures. More TEM images and their Fourier transforms are provided in Fig. S5.†

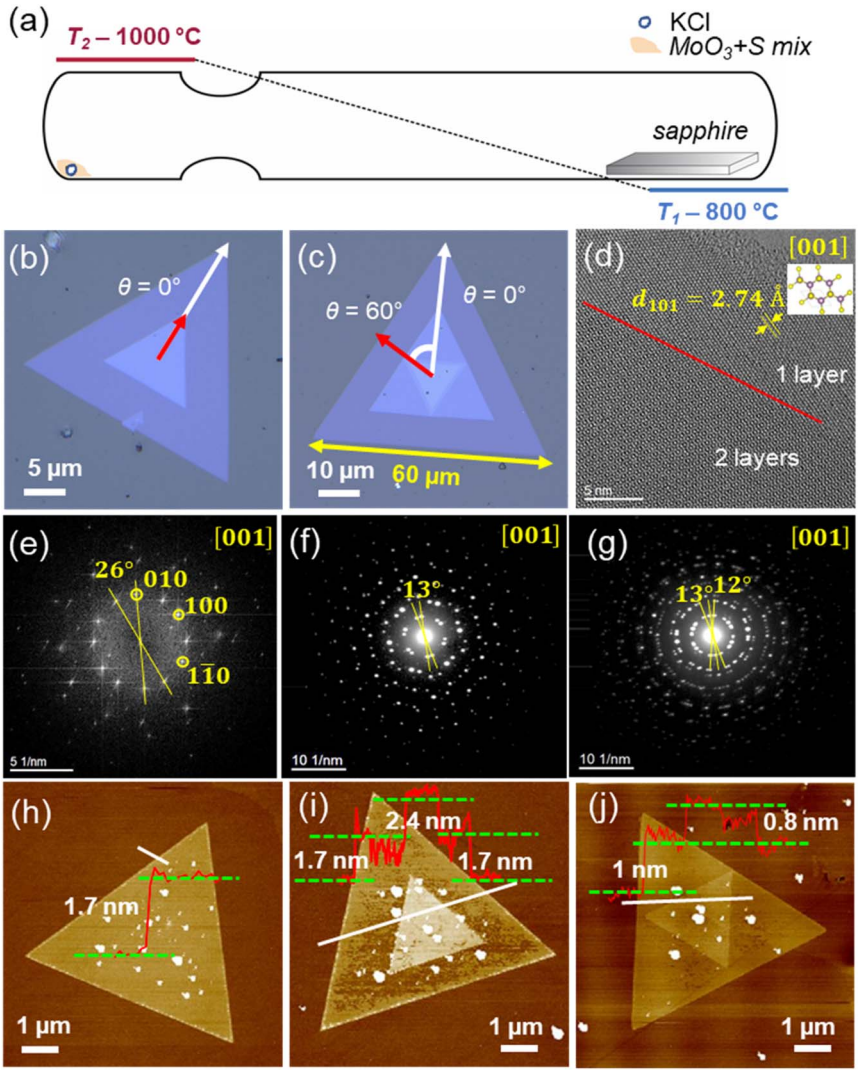

Fig. 3 (a) Schematic CVT setup for growth of MoS_2 nanostructures (heating rate 10 K min^{-1}, $T_2 = 1000$ °C, $T_1 = 800$ °C, $t = 30$ min, naturally cooling). (b and c) Optical microscopy images of twisted MoS_2 stacked in different sizes on a *c*-sapphire (0001) substrate. (d) HRTEM image recorded at the edge of a similar MoS_2 flake at the 001 zone axis. The inset shows the unit cell in this orientation, where Mo is purple and S is yellow. The red line highlights the edge of a second layer twisted by 26° with respect to the first one. (e) Fourier transform of (d) with indexed reflection and the indicated twist angle between the two layers. (f and g) Electron diffraction patterns oriented along the 001 zone axis (hexagonal space group 194) of the same nanoflake at areas where two (f) and three (g) twisted layers are present. AFM images and height profile measurements of different MoS_2 crystals along the marked white line showing three different shapes: triangular (h), parallel (0°) (i), and anti-parallel (60°) (j).

The crystal thicknesses were determined by AFM measurements (Fig. 3h–j). Triangular shapes with a thickness of 1.7 nm are observed, corresponding to three layers (Fig. 3h). Parallel-oriented triangular nanosheets formed on top of the triangular MoS_2 crystal, are also found to exhibit thicknesses of 1.7 nm, corresponding to three layers, or 2.4 nm, corresponding to four layers (Fig. 3i). Anti-parallel oriented nanosheets are found to have a thickness of 0.8 nm, corresponding to a MoS_2 monolayer (Fig. 3j). The AFM images also provide a detailed topographical view of the nanosheets, on the one hand clearly showing the step heights corresponding to the different thicknesses. On the other hand, these high-resolution images highlight the uniformity and smoothness of the nanosheets.

Growth of $CrCl_3/MoS_2$ heterostructures

In a second step, $CrCl_3/MoS_2$ heterostructures were prepared and analyzed. The sequential CVT approach involved the deposition of $CrCl_3$ (as a top layer) in a vertical orientation on MoS_2, which had already been grown on a *c*-sapphire (0001) substrate (see Fig. 4 and S8†). Here, purified $CrCl_3$ (purification process described in Table S1†) was used. The growth conditions can be described as follows: $T_1 = 500$ °C; $T_2 = 600$ °C and quenched after 5, 10 or 15 min in tap water using an ampoule catcher.[35] The $CrCl_3$ crystals have a hexagonal shape with very sharp edges and exhibit colors ranging from blue to violet depending on their thickness. The $CrCl_3$ crystals were precisely aligned with the MoS_2 layer so that heterostructures were

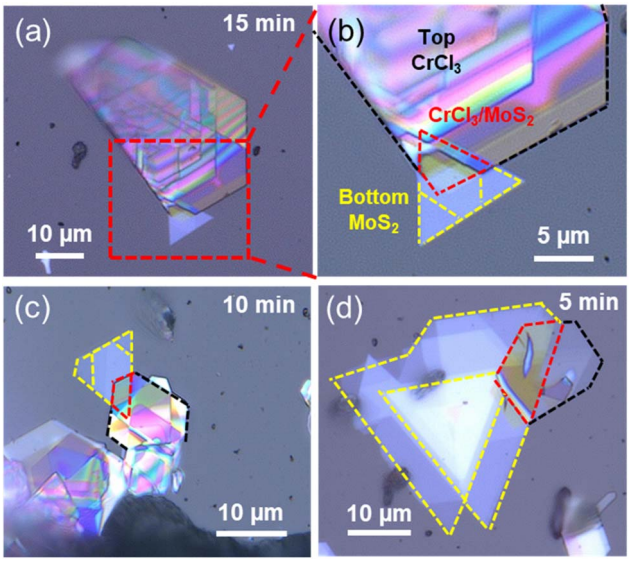

Fig. 4 Optical microscope images of $CrCl_3/MoS_2$ heterostructures prepared by sequential CVT. (a) $CrCl_3/MoS_2$ heterostructure with an ~5 nm $CrCl_3$ layer in the overlapped region ($CrCl_3$ was quenched after 15 min). (b) Zoomed-in view of the area marked in (a). (c) $CrCl_3/MoS_2$ heterostructure ($CrCl_3$ was quenched after 10 min). (d) $CrCl_3/MoS_2$ heterostructure ($CrCl_3$ was quenched after 5 min), illustrating the uniformity and alignment of the layers stacked atop each other (MoS_2 trigonal shapes with yellow dashed lines and $CrCl_3$ hexagonal shapes with black dashed lines).

realized. EDX measurements confirming the composition of $CrCl_3$ are provided in Fig. S7.† The thickness of $CrCl_3$ crystals depends on the quenching time. After 5 min of quenching, $CrCl_3$ crystals with a thickness of approximately 15 nm were obtained. If the ampoule is quenched after 2 hours or more, the $CrCl_3$ crystals grow to over 200 nm in thickness. Thus, by varying the CVT conditions, the thickness of the $CrCl_3/MoS_2$ heterostructure can be controlled.

Characterization of the $CrCl_3/MoS_2$ heterostructure

AFM images of a selected $CrCl_3/MoS_2$ heterostructure were taken to determine their thickness. The thickness of the MoS_2 layer was determined to be 1.4 nm, corresponding to a bilayer, and the $CrCl_3$ layer thickness was found to be 33 nm, corresponding to a multilayer stack, as shown in Fig. 5a. In another sample, shown in Fig. 5b, the thicknesses of the MoS_2 and $CrCl_3$ layers were found to be 11 nm and 14 nm, respectively. Clear step edges in the height profile, observed when crossing from the MoS_2 layer to the $CrCl_3$ layer, indicate that $CrCl_3$ typically forms a flat stack on MoS_2.

Raman measurements were conducted on the as-grown MoS_2 and $CrCl_3$ layers, as well as the $CrCl_3/MoS_2$ heterostructure (as illustrated in Fig. 6 and Fig. S9†). The spectra were obtained from different regions, including MoS_2, $CrCl_3$, and the $CrCl_3/MoS_2$ heterostructure. The top blue spectrum, representing only MoS_2, exhibits two prominent peaks corresponding to the E^1_{2g} and A_{1g} vibration modes of 2H-MoS_2. These peak positions are consistent with previous reports,[41,42] and corroborate our obtained TEM results. The black spectrum at the bottom

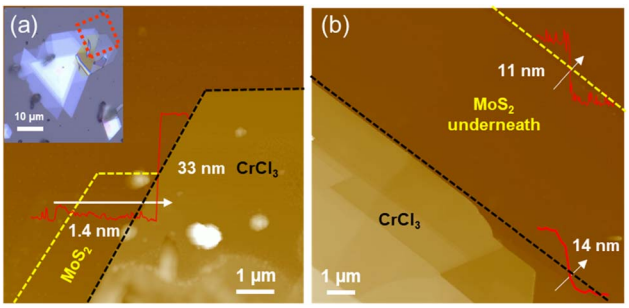

Fig. 5 (a) AFM images of the $CrCl_3/MoS_2$ heterostructure for the marked region in the optical microscope image (inset in (a)). (b) AFM image of another $CrCl_3/MoS_2$ heterostructure. Inset: height profile along the white arrow, shown with the same *x*-scale as the image scale.

displays six modes that align with the monoclinic phase of the synthesized $CrCl_3$ crystals.[16] The middle red spectrum, recorded from the $CrCl_3/MoS_2$ heterostructure region, shows all characteristic peaks of both $CrCl_3$ and MoS_2.

Interestingly, no shift in the Raman modes was observed in the heterostructure region compared to the individual layers. Typically, the formation of a heterostructure results in interlayer charge transfer and strain to achieve potential equilibrium and compensate for lattice mismatch at the interface, which often modifies the properties of the individual layers.[12,19] However, the absence of a shift in the E^1_{2g} and A^1_g modes suggests that the underlying MoS_2 layer remains unaffected by strain and charge doping during the growth process. Similarly, the lack of apparent shift in the Raman modes of $CrCl_3$ indicates a minimal amount of strain in $CrCl_3$ due to lattice mismatch. So, this new synthesis approach can pave the way for innovative advances in growing nanostructures.

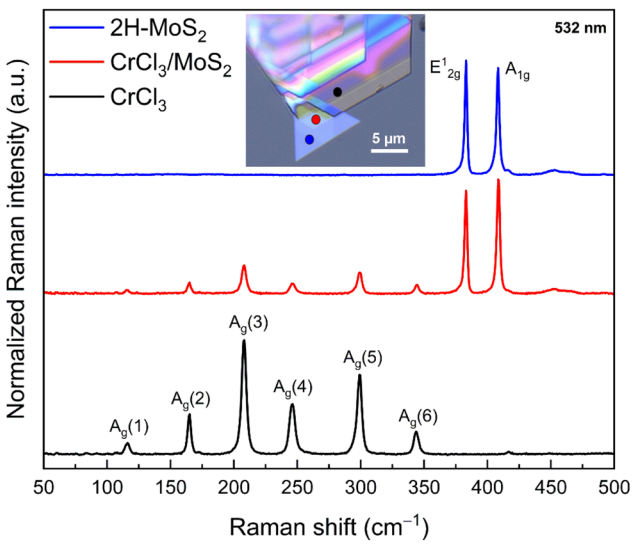

Fig. 6 Raman spectra of the $CrCl_3/MoS_2$ vertical heterostructure. Raman spectra recorded from the three different regions, labelled in the inset optical microscope image of $CrCl_3/MoS_2$, showing the antiparallel triangles of MoS_2, and $CrCl_3$ on the top. There are overlapping Raman signatures with MoS_2 (red line).

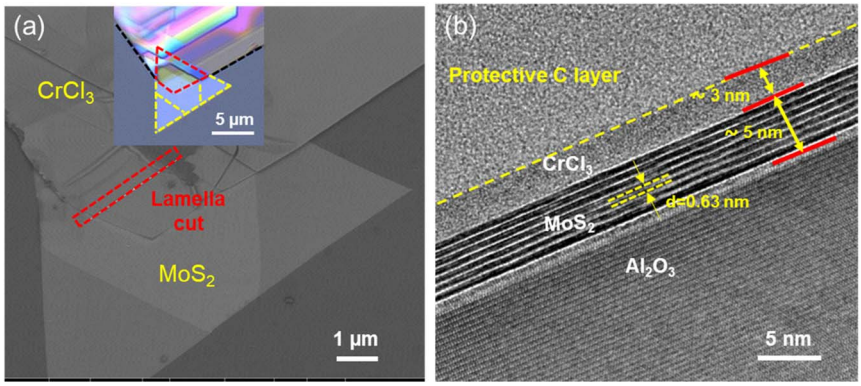

Fig. 7 Structural characterization of the $CrCl_3/MoS_2$ heterostructure. (a) SEM image of the $CrCl_3/MoS_2$ heterostructure, highlighting the marked region for lamella cutting, with the corresponding optical microscope image (inset in (a)). (b) Cross-sectional HRTEM image of a vertically-staked $CrCl_3/MoS_2$ heterostructure. The image shows the distinct layers of MoS_2 and $CrCl_3$, highlighting their interface and alignment.

This stability in the Raman signal suggests that the semiconductor properties of MoS_2 remain intact even after $CrCl_3$ deposition. The preservation of the characteristic Raman peaks and their intensities indicates that the heterostructure retains the high crystalline quality and integrity of both the MoS_2 and $CrCl_3$ layers. This result confirms that the sequential CVT technique allows for the successful assembly of $CrCl_3/MoS_2$ heterostructures without affecting the crystallinity of MoS_2.

The SEM and cross-sectional HRTEM images of the $CrCl_3/MoS_2$ heterostructure (Fig. S10† and 7) depict how the different layers are attached to each other and the Al_2O_3 substrate. In Fig. 7, the 5 nm thin atomically flat 2H-MoS_2 layer is most clearly visible, showing no indications of lattice impurities and point defects. The separation between different vdW layers remained intact and the d_{003}-spacing between them was determined to be 0.63 nm. On top, an ~3 nm thick layer of $CrCl_3$ is identified, reflecting successful heterostructure formation. The hardness of the insulating Al_2O_3 substrate required the use of a higher voltage, *i.e.*, ion energy during FIB cutting. This process unfortunately amorphized the $CrCl_3$ layer whereas MoS_2 was more stable during this process. Additionally, $CrCl_3$ presents a significant challenge due to its susceptibility to damage when exposed to high-energy electron beams and intense laser excitation.[43]

Conclusions

In this study, the synthesis and characterization of $CrCl_3/MoS_2$ vdW heterostructures were comprehensively investigated on *c*-sapphire substrates using a thermodynamically optimized sequential CVT process. The realized structures of MoS_2 exhibit heights down to about 0.8 nm and several μm in lateral size, as measured by AFM. Notably, some of these crystals are randomly twisted by different angles in the range of ~0° to ~60°. The majority of $CrCl_3$ nanosheets exhibit a thickness ranging from 3 to 35 nm, as determined statistically by AFM for several $CrCl_3$ crystals, with large lateral dimensions distributed across the substrate. Notably, thicker crystals are predominantly observed at the substrate edges, with some also present near the center. High-crystallinity and structural quality of both layers were confirmed through Raman spectroscopy and HRTEM. Interestingly, no shift in the Raman modes was observed in the heterostructure, which would typically appear due to strain and interlayer charge transfer to compensate for the lattice mismatch at the interface. These kinds of heterostructures create an optimistic outlook in studying some of the interesting physical properties, *e.g.*, magnetic proximity effects in TMDCs. Our method preserves structural integrity, promoting long spin and exciton lifetimes for use in quantum computing and secure communication technologies.

Data availability

The data supporting this article have been included as part of the ESI.†

Author contributions

Mahmoud M. Hammo: conceptualization, investigation, data curation, visualization, and original draft – writing – review & editing. Samuel Froeschke: simulation, – review & editing. Golam Haider: scientific discussion, and helped in modifying the manuscript in the publication form. Daniel Wolf: TEM measurements and analysis. Alexey Popov: Raman measurements. Bernd Büchner: supervision and proof reading. Michael Mertig: resources, acquisition, supervision and proof reading. Silke Hampel: conceptualization, resources, acquisition, and supervision. All authors have given approval to the final version of the manuscript.

Conflicts of interest

The authors declare that there are no competing interests.

Acknowledgements

The authors express their gratitude to Sandra Nestler for substrate cutting, Volker Neu and Dennis Hofmann for

assistance with AFM measurements, Sandra Schiemenz and Marco Rosenkranz for conducting Raman spectroscopy, Gesine Kreutzer for aiding with EDX quantification, Robert Heider and Katrin Wruck for their laboratory support, and Almut Pöhl for FIB cutting. Daniel Wolf acknowledges financial support from the Collaborative Research Center "Chemistry of Synthetic 2D Materials" funded by the Deutsche Forschungsgemeinschaft (DFG, German Research Foundation) – SFB-1415 (417590517). Mahmoud M. Hammo expresses gratitude to the IFW excellence program for its financial assistance. Mahmoud M. Hammo and Michael Mertig acknowledge financial support from the Deutsche Forschungsgemeinschaft (DFG; RTG 2767).

References

1 J. Yao, Z. Zheng and G. Yang, *Adv. Funct. Mater.*, 2017, **27**, 1701823.
2 H. Zhang, X. Zhang, C. Liu, S.-T. Lee and J. Jie, *ACS Nano*, 2016, **10**, 5113–5122.
3 C. Zhong, V. K. Sangwan, C. Wang, H. Bergeron, M. C. Hersam and E. A. Weiss, *J. Phys. Chem. Lett.*, 2018, **9**, 2484–2491.
4 R. K. Biroju, D. Das, R. Sharma, S. Pal, L. P. Mawlong, K. Bhorkar, P. Giri, A. K. Singh and T. N. Narayanan, *ACS Energy Lett.*, 2017, **2**, 1355–1361.
5 S. Bettis Homan, V. K. Sangwan, I. Balla, H. Bergeron, E. A. Weiss and M. C. Hersam, *Nano Lett.*, 2017, **17**, 164–169.
6 A. K. Geim and I. V. Grigorieva, *Nature*, 2013, **499**, 419–425.
7 B. Tian, Ph.D. Dissertation, King Abdullah University of Science and Technology, 2022.
8 S. K. Behera, M. Bora, S. S. P. Chowdhury and P. Deb, *Phys. Chem. Chem. Phys.*, 2019, **21**, 25788–25796.
9 D. Ghazaryan, M. T. Greenaway, Z. Wang, V. H. Guarochico-Moreira, I. J. Vera-Marun, J. Yin, Y. Liao, S. V. Morozov, O. Kristanovski and A. I. Lichtenstein, *Nat. Electron.*, 2018, **1**, 344–349.
10 Q. Zhang, S. A. Yang, W. Mi, Y. Cheng and U. Schwingenschlögl, *Adv. Mater.*, 2016, **28**, 7043–7047.
11 M.-C. Heißenbüttel, T. Deilmann, P. Krüger and M. Rohlfing, *Nano Lett.*, 2021, **21**, 5173–5178.
12 L. Ciorciaro, M. Kroner, K. Watanabe, T. Taniguchi and A. Imamoglu, *Phys. Rev. Lett.*, 2020, **124**, 197401.
13 A. Rasmita and W.-b. Gao, *Nano Res.*, 2021, **14**, 1901–1911.
14 X. Cai, T. Song, N. P. Wilson, G. Clark, M. He, X. Zhang, T. Taniguchi, K. Watanabe, W. Yao and D. Xiao, *Nano Lett.*, 2019, **19**, 3993–3998.
15 M. A. McGuire, G. Clark, K. Santosh, W. M. Chance, G. E. Jellison Jr, V. R. Cooper, X. Xu and B. C. Sales, *Phys. Rev. Mater.*, 2017, **1**, 014001.
16 D. R. Klein, D. MacNeill, Q. Song, D. T. Larson, S. Fang, M. Xu, R. A. Ribeiro, P. C. Canfield, E. Kaxiras and R. Comin, *Nat. Phys.*, 2019, **15**, 1255–1260.
17 J. Zhao, X. Jin, H. Zeng, C. Yao and G. Yan, *Appl. Phys. Lett.*, 2021, **119**, 213101.
18 K. L. Seyler, D. Zhong, B. Huang, X. Linpeng, N. P. Wilson, T. Taniguchi, K. Watanabe, W. Yao, D. Xiao and M. A. McGuire, *Nano Lett.*, 2018, **18**, 3823–3828.
19 T. P. Lyons, D. Gillard, A. Molina-Sánchez, A. Misra, F. Withers, P. S. Keatley, A. Kozikov, T. Taniguchi, K. Watanabe, K. S. Novoselov, J. Fernández-Rossier and A. I. Tartakovskii, *Nat. Commun.*, 2020, **11**, 6021.
20 J. Choi, C. Lane, J.-X. Zhu and S. A. Crooker, *Nat. Mater.*, 2023, **22**, 305–310.
21 Ł. Kipczak, Z. Chen, P. Huang, K. Vaklinova, K. Watanabe, T. Taniguchi, A. Babiński, M. Koperski and M. R. Molas, *arXiv*, 2023, preprint, arXiv:2304.11896, DOI: **10.48550/arXiv.2304.11896**.
22 J. F. Sierra, J. Fabian, R. K. Kawakami, S. Roche and S. O. Valenzuela, *Nat. Nanotechnol.*, 2021, **16**, 856–868.
23 X. Yin, C. S. Tang, Y. Zheng, J. Gao, J. Wu, H. Zhang, M. Chhowalla, W. Chen and A. T. Wee, *Chem. Soc. Rev.*, 2021, **50**, 10087–10115.
24 P. Rivera, J. R. Schaibley, A. M. Jones, J. S. Ross, S. Wu, G. Aivazian, P. Klement, K. Seyler, G. Clark and N. J. Ghimire, *Nat. Commun.*, 2015, **6**, 6242.
25 D. Zhong, K. L. Seyler, X. Linpeng, N. P. Wilson, T. Taniguchi, K. Watanabe, M. A. McGuire, K.-M. C. Fu, D. Xiao, W. Yao and X. Xu, *Nat. Nanotechnol.*, 2020, **15**, 187–191.
26 C. Boix-Constant, S. Mañas-Valero, R. Córdoba, J. J. Baldoví, Á. Rubio and E. Coronado, *ACS Nano*, 2021, **15**, 11898–11907.
27 Y. Xia, J. Zha, H. Huang, H. Wang, P. Yang, L. Zheng, Z. Zhang, Z. Yang, Y. Chen and H. P. Chan, *ACS Appl. Mater. Interfaces*, 2023, **15**(29), 35196–35205.
28 J. McKenzie, N. Sharma and X. Liu, *APL Mater.*, 2024, **12**, 070602.
29 A. V. Kretinin, Y. Cao, J.-S. Tu, G. Yu, R. Jalil, K. S. Novoselov, S. J. Haigh, A. Gholinia, A. Mishchenko and M. Lozada, *Nano Lett.*, 2014, **14**, 3270–3276.
30 F. Liu, *Prog. Surf. Sci.*, 2021, **96**, 100626.
31 Y. Gong, J. Lin, X. Wang, G. Shi, S. Lei, Z. Lin, X. Zou, G. Ye, R. Vajtai and B. I. Yakobson, *Nat. Mater.*, 2014, **13**, 1135–1142.
32 S. Hao, X. Ji, F. Liu, S. Zhong, K. Y. Pang, K. G. Lim, T. C. Chong and R. Zhao, *ACS Appl. Nano Mater.*, 2021, **4**, 1766–1775.
33 R. Ai, X. Guan, J. Li, K. Yao, P. Chen, Z. Zhang, X. Duan and X. Duan, *ACS Nano*, 2017, **11**, 3413–3419.
34 C. W. Bale, E. Bélisle, P. Chartrand, S. A. Decterov, G. Eriksson, A. E. Gheribi, K. Hack, I. H. Jung, Y. B. Kang, J. Melançon, A. D. Pelton, S. Petersen, C. Robelin, J. Sangster, P. Spencer and M. A. Van Ende, *Calphad*, 2016, **54**, 35–53.
35 M. Grönke, B. Buschbeck, P. Schmidt, M. Valldor, S. Oswald, Q. Hao, A. Lubk, D. Wolf, U. Steiner and B. Büchner, *Adv. Mater. Interfaces*, 2019, **6**, 1901410.
36 S. Froeschke, D. Wolf, M. Hantusch, L. Giebeler, M. Wels, N. Gräßler, B. Büchner, P. Schmidt and S. Hampel, *Nanoscale*, 2022, **14**, 10483–10492.

37 S. Froeschke, N. Yasmen, A. A. Popov, S. Schiemenz, D. Wolf, L. Giebeler, M. Hantusch, N. Gräßler, B. Büchner and P. Schmidt, *Chem. Mater.*, 2023, **35**, 4136–4148.
38 H. Schäfer, *Angew Chem. Int. Ed. Engl.*, 1976, **15**, 713–727.
39 S. Lopatin and S. Shugurov, *Russ. J. Gen. Chem.*, 2019, **89**, 1059–1068.
40 J. Barthel, *Ultramicroscopy*, 2018, **193**, 1–11.
41 H. Cun, M. Macha, H. Kim, K. Liu, Y. Zhao, T. LaGrange, A. Kis and A. Radenovic, *Nano Res.*, 2019, **12**, 2646–2652.
42 C. Lee, H. Yan, L. E. Brus, T. F. Heinz, J. Hone and S. Ryu, *ACS Nano*, 2010, **4**, 2695–2700.
43 J. Wang, Z. Ahmadi, D. Lujan, J. Choe, T. Taniguchi, K. Watanabe, X. Li, J. E. Shield and X. Hong, *Adv. Sci.*, 2023, **10**, 2203548.